PAPER

Check for updates

Design and synthesis of coumarin-based pyrazole–pyrazoline hybrid derivatives and their photophysical, antimicrobial, sensing and computational studies

Neelam Sharma,[a] Aman Kumar,[a] Ved Prakash Verma, [b] Madhur Babu Singh,[c] Prashant Singh [c] and Rahul Shrivastava [*a]

In recent times, nitrogen-containing multi-heterocyclic compounds have emerged as valuable scaffolds in the field of medication development because of their broad spectrum of biological activities. In this context, we designed and synthesized new multi-heterocyclic coumarin-based pyrazole–pyrazoline hybrids (**4a–4r**) through a molecular hybridization approach. The green metrics assessment results revealed that the current molecular hybridization approach is environmentally benign and provides excellent green certification for a safe and sustainable environment. After successful structural characterization, all compounds were evaluated for their antimicrobial potential against various microbial strains. The results of antimicrobial studies showed that compound **4c** was most active against *B. subtilis* and *A. niger*, with MICs of 0.0132 and 0.0265 µmol mL^{-1}, respectively. To understand the plausible mechanism responsible for the antimicrobial action of the synthesized compounds, molecular docking studies were performed. Furthermore, the sensing behaviours of multi-heterocyclic molecules (**4a–4r**) were evaluated, and the results revealed that most of the derivatives detected Cu^{2+}, Ce^{4+} and Hg^{2+} metal ions in nanomolar detection limits. The Job's and B–H plots demonstrated that these compounds interact with Cu^{2+}, Ce^{4+} and Hg^{2+} ions in ratios of 1 : 1, 1 : 2 and 2 : 1 binding stoichiometry, respectively.

Introduction

Heterocyclic compounds are exceptionally important for the lifecycles of several living organisms since their presence in living cells in different forms plays a significant role in numerous biological processes.[1,2] Additionally, heterocyclic compounds serve as an important scaffold in the field of drug development because of their medicinal and pharmacological properties. For example, oxygen-, nitrogen- and sulphur-containing heterocyclic compounds are generally utilized as a basic skeleton of numerous pharmaceutically significant drug molecules.[3] In recent times, chemists and biologists globally have shown their immense interest in electron-rich nitrogen-containing heterocyclic compounds because of their valuable biological potentials and versatile nature, which make them extremely useful compounds.[4,5] Nitrogen-containing heterocyclic compounds are a structural part of a wide range of natural products, such as hormones, vitamins, alkaloids, and antibiotics, which exhibit several medicinal, chemical and biological applications.[6,7] Among N-heterocycles, five-membered pyrazole hybrids with two adjacent nitrogen atoms in the cyclic ring have attracted the noteworthy attention of medicinal chemists in the last few decades due to their wide spectrum of biological activities, such as antianxiety, anti-fungicidal, anti-inflammatory, antimicrobial, and antimalarial activities, and are also used in biodegradable agrochemicals.[8–14] The dihydro derivative of pyrazole is known as pyrazoline, another fascinating heterocyclic synthon used in the design of new lead drug molecules, as it exhibits a plethora of biological activities. The literature reveals that pyrazolines exist as 1-pyrazolines, 2-pyrazolines, and 3-pyrazolines depending on the position of the double bond. Among these three derivatives, 2-pyrazolines are more useful in the pharmaceutical and medicinal sectors because of their high stability.[15,16] The 2-pyrazolines and their derivatives are also used as isosteres of imidazole, thiazole, tetrazole, oxazole, triazole and isoxazole heterocyclic scaffolds as they have exceptional ability to modulate their biological profile and physicochemical properties that highlight the versatility of 2-pyrazolines as isosteres of different heterocycles.[17,18] Therefore, 2-pyrazoline and its derivatives have been extensively explored by medicinal chemists and biologists to

[a]Department of Chemistry, Manipal University Jaipur, VPO-Dehmi-Kalan, Off Jaipur Ajmer Express Way, Jaipur, Rajasthan, 303007, India. E-mail: chem.rahul@gmail.com; rahul.shrivastava@jaipur.manipal.edu

[b]Department of Education in Science and Mathematics, Regional Institute of Education, Bhubaneshwar, India

[c]Department of Chemistry, Atma Ram Sanatan Dharma College, University of Delhi, New Delhi, India

combat a wide variety of diseases.[19–21] The detail literature analysis revealed that 2-pyrazolines and related derivatives possess versatile biological profiles, such as anticonvulsant,[22] anticancer,[23] antibacterial,[24] antimalarial, antifungal,[25] anti-depressant,[26] anti-inflammatory, anti-amoebic,[27] monoamine oxidase (MAO) inhibitory,[28] anti-parkinsonian,[29] cholines-terase,[30] aldose reductase,[31] carbonic anhydrase (CA),[32] canna-binoid CB1,[33] and EGFR tyrosine kinase inhibitory activities.[34] The structural activity relationship studies indicate that varia-tion in functional groups substituted with 2-pyrazoline usually generates a positive impact on its biological potential. The importance of pyrazolines as bioactive scaffolds is reflected by their presence in several marketed drugs, such as phenylbuta-zone, antipyrine, ramifenazone, famprofazone, morazone, metamizole, aminophenazone, edaravone, sulfinpyrazone, ibi-pinabant and axitinib, used for the treatment of various diseases, as depicted in Fig. 1.[35] Several synthetic methodolo-gies have been adopted for the synthesis of structurally diverse 2-pyrazolines and their derivatives, but common and frequently used methodologies for synthesis of 2-pyrazolines are (a) reac-tion of carboxylic acid esters and α,β-enones with diazoalkane; (b) reaction of α,β-unsaturated aldehydes and ketones with hydrazines; and (c) reaction of olefins and α,β-enones with nitrilimines. In these approaches, nitrogen atoms originate from reactants, such as diazoalkanes, hydrazines and nitrili-mines, respectively.[36] Furthermore, hydrazines and their deriv-atives are the most frequently used reactants as a source of

nitrogen atoms in the 2-pyrazoline ring. Along with pyrazoles and pyrazolines, coumarin (2H-1-benzopyran-2-one) represents a privileged class of bioactive molecules with a wide spectrum of biological applications and peculiar physicochemical features that are useful for medication development. Generally, coumarin originates from plants and exhibits diverse pharma-cological activities, like anti-HIV, anticoagulant, antibacterial, antihypertensive, antioxidant, antifungal, antitubercular, anti-hyperglycemic, and anti-inflammatory scavenging of reactive oxygen species. The therapeutic applications of coumarins mostly depend on the nature and pattern of substituted func-tional groups in the basic nucleus.[37]

The molecular hybridization strategy is one of the most rationally attractive approaches used in the design and construction of innovative bioactive agents. It involves the integration of two or more distinct active pharmacophoric heterocyclic moieties usually via a spacer or linker in the same molecule to form a new multi-heterocyclic molecular hybrid with potentially higher efficacy and activity compared to the parent heterocyclic moieties and alleviated side effects of a single biologically active heterocyclic entity. Insights from a literature survey revealed the medicinal and biological importance of heterocyclic entities derived from hybrid mole-cules associated with an array of biological functions. For instance, multi-heterocyclic hybrid molecules (such as hybrid molecules of coumarin with furane, isatin, pyrrole, thiazoles, triazolo-thiazoles, triazolo-thiadiazines, thiazolidines, oxazole,
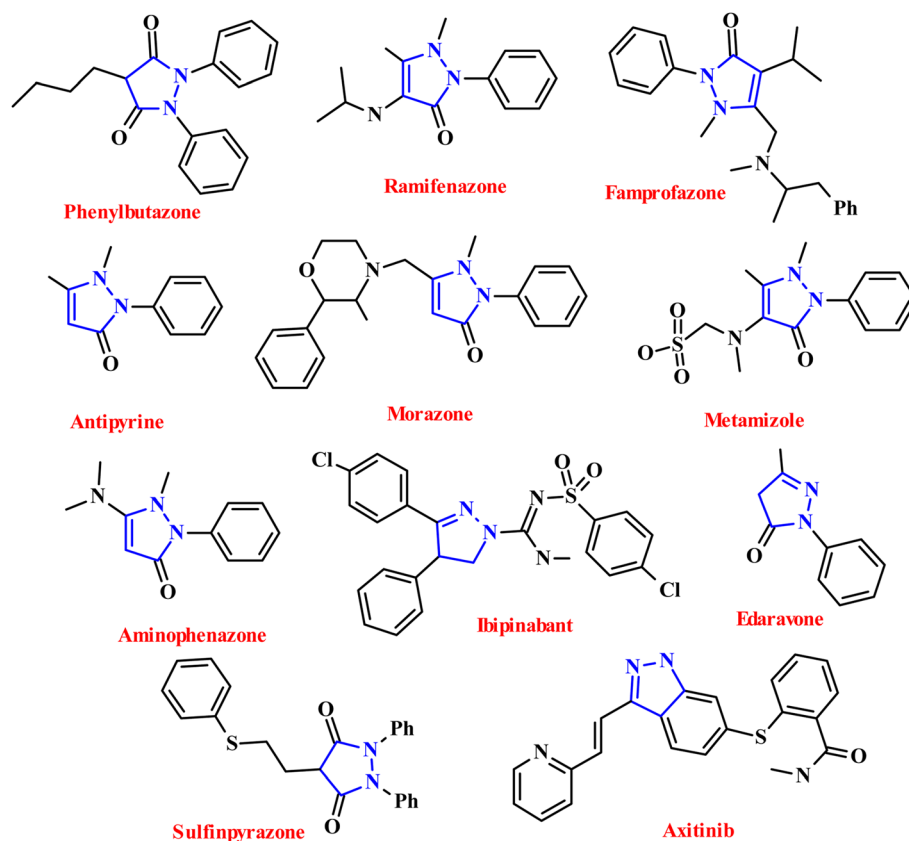

Fig. 1 Chemical structures of pyrazoline-based clinically used commercial drugs.

quinoxaline, and quinoline); hybrid molecules of pyrazole with pyridine, pyrimidine, pyrazoles, oxadiazole, chalcone, diazepine, imidazopyridazine, and benzothiazole; and hybrid compounds of pyrazoline with quinoline, pyridine, oxazole, thiophene, pyrazole, and thymol have been extensively reported to have remarkable inhibitory potential in recent years.[38–40] In view of literature findings and keeping in view the therapeutic potential of coumarin, pyrazole and pyrazoline moieties, we planned to synthesize new multi-heterocyclic hybrid compounds, which involve the insertion of these bioactive moieties into a single heterocyclic framework that may demonstrate useful multi biological activities *via* a synergistic effect. To the best of our knowledge, in this area, the synthesis of multi-heterocycles combined with coumarin, pyrazole and pyrazoline has rarely been reported for active medicinal applications.[41] Therefore, in this study, we reported the synthesis of coumarin–pyrazole-linked pyrazoline derivatives using a molecular hybridization approach and their spectroscopic studies, green chemistry metric analysis, antimicrobial, molecular docking and sensing studies towards metal ions.
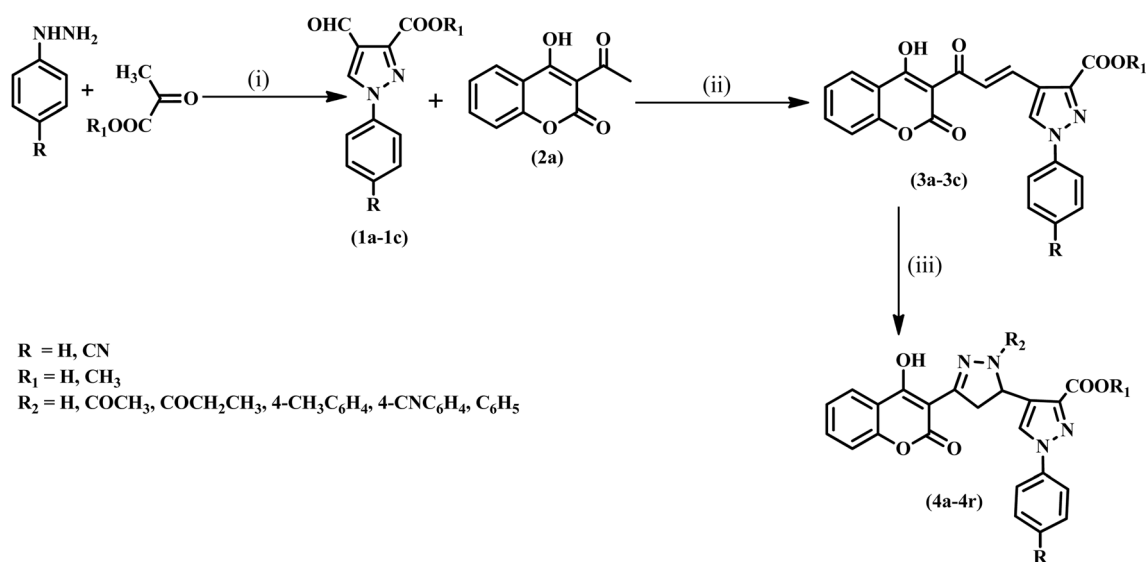
Materials and apparatus

Analytical grade chemicals and solvents, hydrazine hydrates, $CHCl_3$, ethanol, CH_3OH, acetic acid, phosphorus oxychloride, and propionic acid were acquired from Merck, India. The Bruker Advance DPX-250 spectrometer was used to record both proton and carbon NMR spectra for analysis. The UV-vis absorbance spectra of the products were recorded using a Shimadzu UV-2600 spectrophotometer, and the fluorescence spectra of the products were recorded using a spectrofluorophotometer. A JASCO FT/IR 4600 spectrophotometer was used to obtain the FT-IR spectra of the synthesized compounds.

Computational details

Molecular docking studies were performed for some selected synthesized coumarin-based pyrazole–pyrazoline hybrid compounds with target proteins using AutoDock Vina.[42] The Protein Data Bank (PDB) RCSB was used for downloading 3D structures of target proteins with their respective PDB IDs (5ZT7, 1N67, 1KZN, 6P8U, 8BBX and 5TZ1). The protein structures were prepared using Chimera by assigning Gasteiger partial charges.[43,44] The structure of the prepared hybrid compounds was drawn using ChemDraw Professional 15.0 and converted into 3D structures using CHEM 3D 15.0.[45] The docking protocol used a Lamarckian genetic algorithm with default parameters for the population size (150), maximum generations (27 000) and maximum energy evaluations (2 500 000). For each ligand–protein complex, the top-scoring pose (lowest binding energy) was chosen for analysis. All docked poses were visualized using Discovery Studio Visualizer.[46,47]
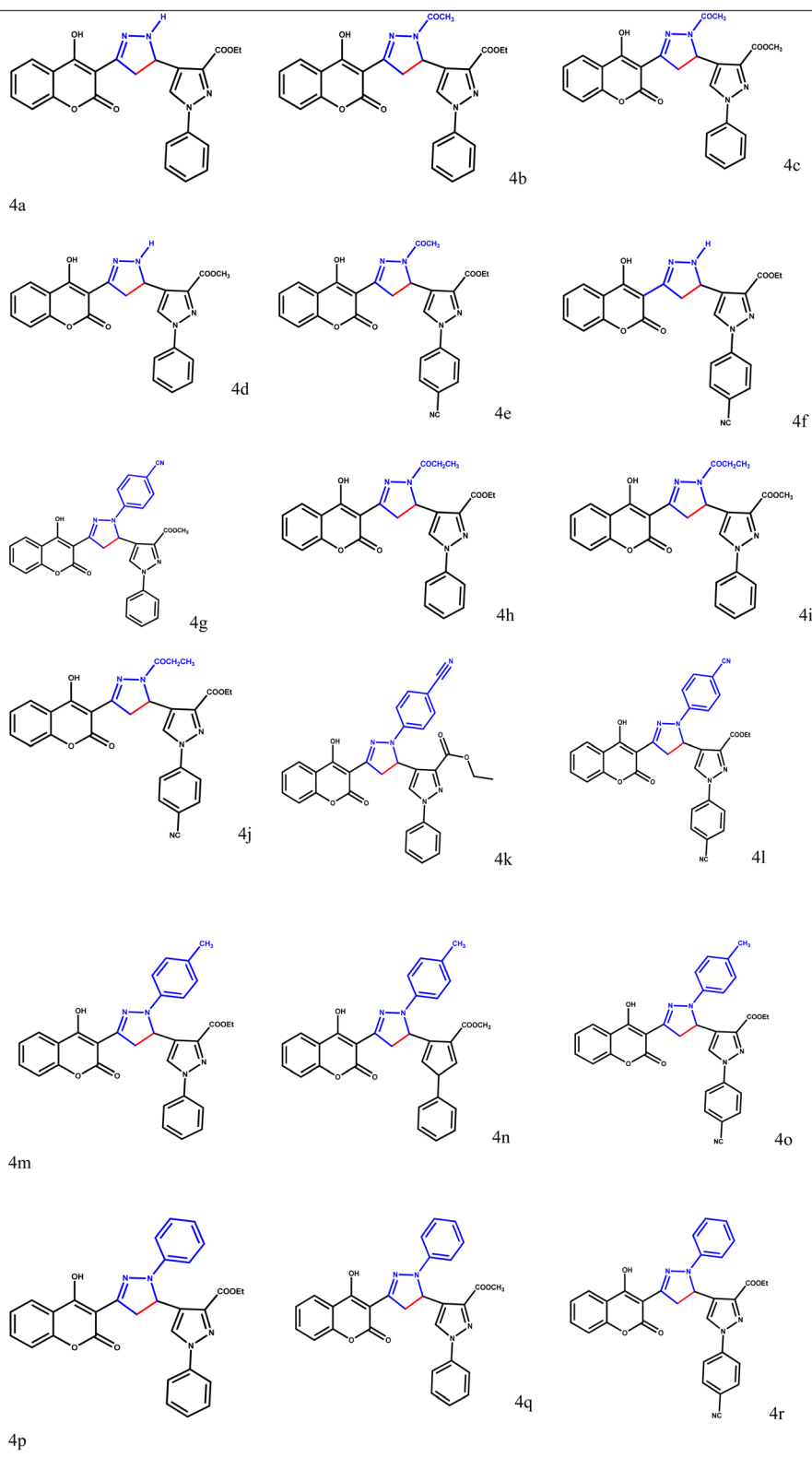
Results and discussion

To synthesize coumarin-based pyrazolepyrazoline hybrids, a multistep synthetic protocol was followed, as depicted in Scheme 1. Initially, alkyl-4-formyl-1-phenyl-1*H*-pyrazole-3-carboxylates (**1a–1c**) were synthesized according to our previously reported methods.[48] Another starting material, 3-acetyl-4-hydroxycoumarin (**2a**), was synthesized in 93% yield by the acetylation reaction of commercially procured 4-hydroxycoumarin using acetic acid and $POCl_3$ at room temperature. Further, chalcones (**3a–3c**) were prepared according to the Claisen–Schmidt reaction between alkyl-4-formyl-1-phenyl-1*H*-pyrazole-3-carboxylates (**1a–1c**) and 3-acetyl-4-hydroxycoumarin (**2a**) in chloroform using piperidine as a basic catalyst in 85% product yield. Finally, coumarin-derived pyrazole–pyrazoline

R = H, CN
R$_1$ = H, CH$_3$
R$_2$ = H, COCH$_3$, COCH$_2$CH$_3$, 4-CH$_3$C$_6$H$_4$, 4-CNC$_6$H$_4$, C$_6$H$_5$

Scheme 1 Systematic representation of the synthesis of coumarin-derived pyrazole–pyrazoline hybrid heterocyclic molecules (**4a–4r**). Reaction conditions: (i) water, TFA, and stir 8–10 h; (ii) chloroform, reflux, and 4–5 h; and (iii) ethanol/acetic acid/propionic acid, reflux, and 3–4 h.

Table 1 Synthesized coumarin-derived pyrazole–pyrazoline hybrid heterocyclic molecules (**4a–4r**)

hybrid heterocyclic molecules (4a–4r) were prepared using chalcones (3a–3c) and various phenyl hydrazine hydrochlorides in three media: ethanol, acetic acid and propionic acid. The chemical structures of the newly synthesized coumarin-derived pyrazole–pyrazoline hybrids (4a–4r) were elucidated using FT-IR, ^{1}H-NMR, ^{13}C-NMR and mass spectral data. The different derivatives of coumarin-derived pyrazole–pyrazoline hybrid heterocyclic molecules (4a–4r) are listed in Table 1.

Antimicrobial activities of coumarin-based pyrazole–pyrazoline hybrid heterocyclic molecules

As reported in the literature, coumarin, pyrazole and pyrazoline derivatives independently exhibit strong antimicrobial potency towards various microbial species. Therefore, considering the antimicrobial potential of these moieties, the synthesized coumarin-based pyrazole–pyrazoline hybrid heterocyclic molecules (4a–4r) were evaluated for antimicrobial potential against various *Bacillus subtilis* (MTCC 421), *Pseudomonas aeruginosa* (MTCC 647), *Staphylococcus aureus* (MTCC 3160), *Escherichia coli* (MTCC 16521), *Aspergillus niger* and *Candida albicans* using a serial dilution protocol. The antibacterial drug ciprofloxacin and antifungal drug fluconazole were utilized as reference drugs to compare the antibacterial and antifungal activities of the synthesized coumarin-based pyrazole–pyrazoline hybrid heterocyclic molecules (4a–4r). These newly derived hybrids were tested for their antimicrobial efficacy at 3.125, 6.25, 12.5, 25 and 50 μg mL^{-1} in DMSO. All assays were performed in triplicate to ensure reproducibility. The results of the antimicrobial assay are tabulated in Table 2.

The results of the antimicrobial study demonstrated that coumarin-based pyrazole–pyrazoline hybrids (4a–4r) displayed the highest efficacy against *B. subtilis* (MIC = 0.0132–0.0876

μmol mL^{-1}) among tested Gram-positive bacterium strains *S. aureus* and *B. subtilis*. The results also showed that hybrid compound 4c was most active against *B. subtilis* with an MIC of 0.0132 μmol mL^{-1}, which was comparable to the activity of ciprofloxacin (MIC = 0.0094 μmol mL^{-1}), while 4o exhibited maximum potency against *S. aureus* (MIC = 0.0223 μmol mL^{-1}). It was observed that most of the synthesized hybrid molecules showed equipotent antimicrobial efficacy for the tested Gram-negative bacterial species. Compound 4d showed maximum potency towards *E. coli* with an MIC of 0.0145 μmol mL^{-1}, while 4b and 4i inhibited the growth of *P. aeruginosa* equally with an MIC of 0.0257 μmol mL^{-1}. All derivatives (4a–4r) showed less efficacy as antifungal agents compared to the antibacterial efficacy of the tested microbes. Derivatives 4a (MIC = 0.0281 μmol mL^{-1}) and 4c (MIC = 0.0265 μmol mL^{-1}) demonstrated maximum potency as antifungal agents against *C. albicans* and *A. niger*, respectively, which is nearly two times better than the potency of fluconazole against these tested fungal strains.

The structure activity analysis was established based on result analyses of antimicrobial and antifungal activities: (a) the inclusion of substituent COCH$_3$ on N-1 of pyrazoline compared to H and COC$_2$H$_5$ led to augmentation in antibacterial activity of compounds having phenyl and COOC$_2$H$_5$ substituents at the N-1 and C-3 positions of pyrazole (4a, 4b, and 4h), while substitution on N-1 of pyrazoline led to a decrease in antifungal activity of compounds 4a, 4b and 4h; (b) the presence of a nitrile group (C≡N) on the pyrazole-linked phenyl ring results in a decrease in the antimicrobial efficacy of the synthesized hybrids with H or COCH$_3$ substituents on N-1 of pyrazoline and COOC$_2$H$_5$ at N-1 of the pyrazole ring of compound 4a, 4b, 4e and 4f; (c) the replacement of COOC$_2$H$_5$ (4a, 4b, 4h, and 4p) on pyrazole ring with COOCH$_3$

Table 2 Antimicrobial and antifungal screening analysis results of coumarin-based pyrazoline hybrids (4a–4r)

Minimum inhibitory concentration (MIC, μmol mL^{-1})

Compounds	*B. subtilis*	*S. aureus*	*E. coli*	*P. aeruginosa*	*A. niger*	*C. albicans*
4a	0.0281	0.0562	0.0281	0.0281	0.0562	0.0281
4b	0.0257	0.0257	0.0257	0.0257	0.1028	0.0514
4c	0.0132	0.0265	0.0265	0.0265	0.0265	0.0529
4d	0.0290	0.0290	0.0145	0.0581	0.0581	0.1162
4e	0.0489	0.0978	0.0978	0.0978	0.1466	0.1466
4f	0.0532	0.1065	0.0532	0.0532	0.1598	0.1598
4g	0.0235	0.0235	0.0235	0.0470	0.1411	0.1411
4h	0.0499	0.0999	0.0999	0.0999	0.0999	0.0999
4i	0.0257	0.0514	0.0514	0.0257	0.1028	0.1028
4j	0.0476	0.0476	0.0476	0.0476	0.0952	0.1427
4k	0.0229	0.0229	0.0458	0.0458	0.1375	0.0916
4l	0.0876	0.0876	0.0438	0.0438	0.1314	0.0876
4m	0.0468	0.0935	0.0468	0.1310	0.1403	0.1403
4n	0.0482	0.0964	0.0482	0.1736	0.1446	0.1446
4o	0.0223	0.0223	0.0223	0.1251	0.0894	0.0447
4p	0.0480	0.0480	0.0480	0.0480	0.0960	0.1345
4q	0.0247	0.0247	0.0494	0.0494	0.0987	0.1481
4r	0.0458	0.0229	0.0916	0.0458	0.0458	0.0458
Ciprofloxacin	0.0094	0.0094	0.0094	0.0094	—	—
Fluconazole	—	—	—	—	0.0408	0.0408

(**4c**, **4d**, **4i**, and **4q**) led to the increase in activity most of the time against *B. subtilis* and *S. aureus*, keeping all other substituents same; (d) the pyrazoline hybrid **4c** with $COCH_3$ and $COOCH_3$ substituents at the N-1 positions of pyrazoline and pyrazole, respectively, with a phenyl ring at C-3 of pyrazole demonstrated maximum potency against *B. subtilis* with an MIC of 0.0132 μmol mL; and (e) no common trend of anti-microbial activity was noticed on substitution of phenyl ring on the N-1 of pyrazoline.

Docking study of coumarin-based pyrazole–pyrazoline hybrid heterocyclic molecules

To gain more insights into the binding interactions of the synthesized coumarin-based pyrazole–pyrazoline hybrids with the target proteins, molecular docking studies were performed. In molecular docking studies, the structures of synthesized compounds were drawn using ChemDraw Professional 15.0 and converted into 3D molecular structures using Chem3D. Each molecule was subjected to geometry optimization through energy minimization using the MM2 force field to obtain the lowest-energy stable conformation. The energy-minimized structures were then saved in mol2 format and used for docking. This process ensured that the structure was selected based on thermodynamic stability, leading to more reliable binding affinity predictions and interaction analyses. Docking was performed using AutoDock Vina, scanning the entire protein surface to identify optimal binding sites. The docking results are not influenced by the specific (*R*) or (*S*) configuration at the C-5 chiral centre. Docking was performed using the (*R*)-enantiomer, which is consistent with experimental antimicrobial data obtained. This is attributed to the scoring function of AutoDock Vina, which evaluates binding based on shape complementarity and interaction energies primarily governed by π–π stacking, hydrophobic contacts and hydrogen bonding involving the coumarin, pyrazole and phenyl moieties.[49,50] These interactions are not highly stereospecific at the C-5 position, as confirmed by preliminary docking runs with both enantiomers. Considering these facts, docking analysis was carried out to monitor the binding affinities and interaction profiles of selected hybrid molecules (**4a**, **4b**, **4c**, **4d**, **4i**, and **4o**) against six target proteins associated with antimicrobial activity: 5ZT7 (*B. subtilis*), 1N67 (*S. aureus*), 1KZN (*E. coli*), 6P8U (*P. aeruginosa*), 8BBX (*A. niger*), and 5TZ1 (*C. albicans*), respectively. These proteins were selected based on their relevance to the

antimicrobial activity of the tested microbial strains. The docking results, including binding energies and interaction profiles, are summarized in Table 3. The more negative values of the free energy of binding indicate a stronger binding affinity. The docking results showed that all compounds exhibited favourable binding affinities, with binding energies ranging from −8.1 to −10.7 kcal mol^{-1} across the target proteins. Compound **4c** has the highest binding affinity against 8BBX (*A. niger*), with a binding energy of −10.7 kcal-mol^{-1}, consistent with its strong antifungal activity (MIC = 0.0265 μmol mL^{-1} against *A. niger*). Similarly, compound **4o** showed the strongest binding to 1N67 (*S. aureus*), with a binding energy of −10.3 kcal mol^{-1}, aligning with its potent antibacterial activity (MIC = 0.0223 μmol mL^{-1} against *S. aureus*). Compound **4a** exhibited the highest affinity for 5TZ1 (*C. albicans*) at −10.1 kcal mol^{-1}, supporting its antifungal efficacy (MIC = 0.0281 μmol mL^{-1} against *C. albicans*). The 2D and 3D docked poses (Fig. 2) provided insights into the molecular interactions driving these affinities. For instance, the docked pose of compound **4c** with 5ZT7 (*B. subtilis*) revealed key hydrogen bonding interactions between the $COCH_3$ group on the pyrazoline ring and polar residues in the active site, which were supplemented by π–π stacking interactions between the coumarin moiety and aromatic residues. Similarly, compound **4o**'s pose with 1N67 (*S. aureus*) showed hydrophobic interactions involving the phenyl ring at the C-3 position of pyrazole, increasing its binding stability. For compound **4d** with 1KZN (*E. coli*), the $COOCH_3$ group formed strong hydrogen bonds with active site residues, contributing to its high binding energy (−9.3 kcal mol^{-1}) and potent activity (MIC = 0.0145 μmol mL^{-1}). The docked poses of compound **4b** with 6P8U, **4c** with 8BBX and **4a** with 5TZ1 are depicted in Fig. S35 (SI). These results indicate that stronger binding affinities correlate with enhanced antimicrobial efficacy, supporting the idea that ligand-protein interactions play an important role in the observed biological activities.

Green chemistry metrics analysis of coumarin-based pyrazole–pyrazoline hybrid heterocyclic molecules

The development of green chemical processes or methodologies is the utmost requirement for a safe and sustainable environment. Therefore, we assessed the green chemistry credentials of synthesized coumarin-based pyrazole–pyrazoline hybrid molecules (**4a–4r**) by preforming green metrics calculations, such as atom economy (AE), atom efficiency (AEf), effective mass yield (EMY), reaction mass efficiency (RME), carbon efficiency (CE), optimum efficiency (OE), process mass intensity (PMI), mass intensity (MI), mass productivity (MP), solvent intensity (SI) and *E*-factor. The high values of atom economy, carbon efficiency, reaction mass efficiency, and effective mass yield (EMY) indicate the minimum use of non-benign reagents and solvents in the reaction along with high product yield. The lower value of process mass intensity, mass efficiency, solvent intensity and *E*-factor specially indicates minimum use of non-benign solvents in the workup procedure during the isolation of the

Table 3 Binding energy (kcal mol^{-1}) of some selected docked coumarin-based pyrazole–pyrazoline hybrids

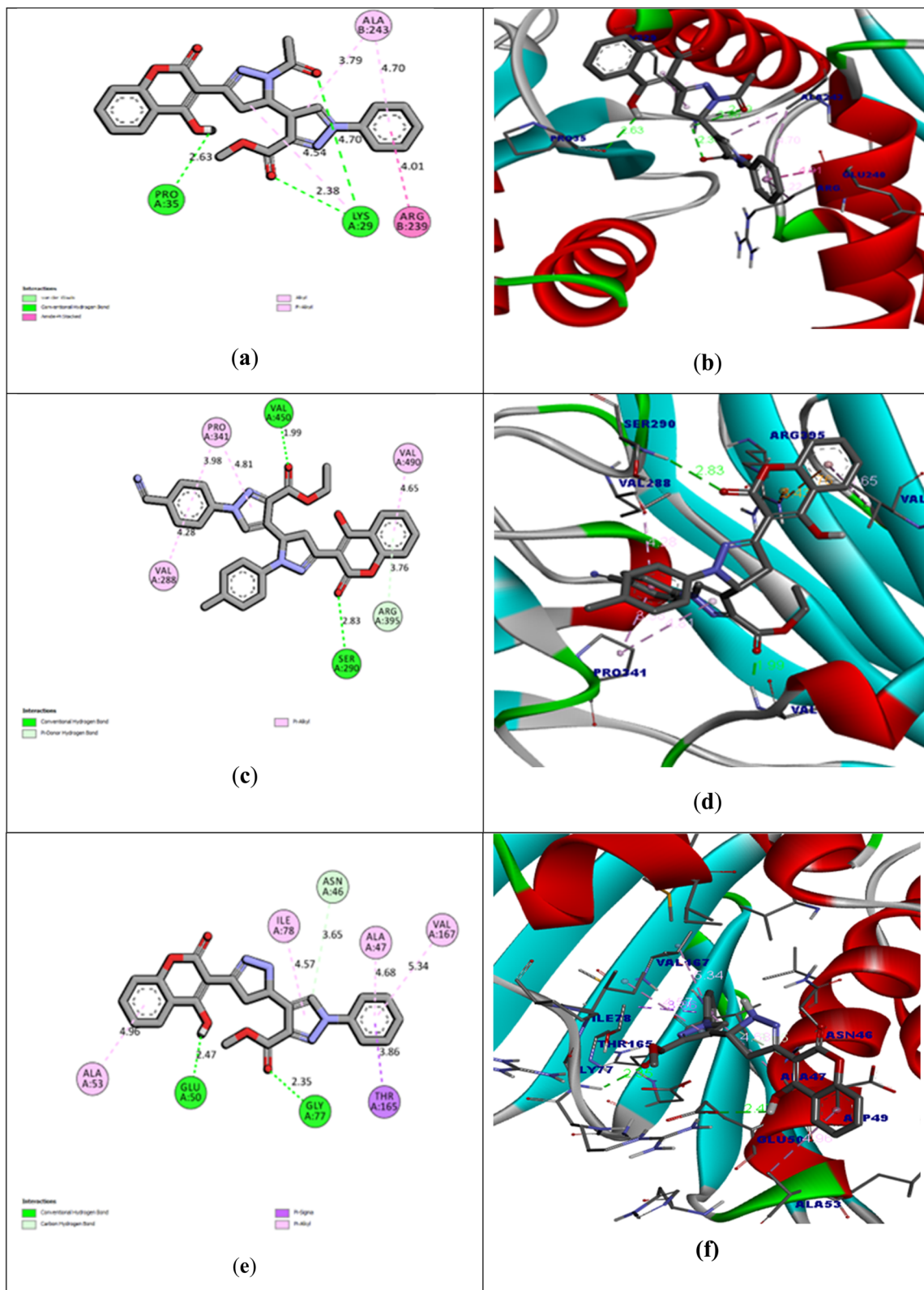| S. no.	Compound	5ZT7	1N67	1KZN	6P8U	8BBX	5TZ1
1	**4a**	−8.1	−9	−8.7	−9.5	−9.6	**−10.1**
2	**4b**	−8.2	−9.9	−9.1	**−9.7**	−9.5	−9.9
3	**4c**	**−8.9**	−10	−9.2	−8.4	**−10.7**	−9.9
4	**4d**	−8.6	−9	**−9.3**	−9	−9.5	−9.7
5	**4i**	−8.3	−10	−8.9	−8.4	−9.3	−9.4
6	**4o**	−8.5	**−10.3**	−9.2	−9.5	−9.9	−10

Fig. 2 Selected docked poses of coumarin-based pyrazole–pyrazoline hybrids: (a) 2D-docked poses of 5ZT7 with **4c**; (b) 3D-docked poses of 5ZT7 with **4c**; (c) 2D-docked poses of 1N67 with **4o**; (d) 3D-docked poses of 1N67 with **4o**; (e) 2D-docked poses of 1KZN with **4d**; and (f) 3D-docked poses of 1KZN with **4d**.

Table 4 Green metrics (EMY, AEf, AE, RME, OE, CE, and MP) of synthesized **4a–4r**[a]

S. no.	Product	Yield (%)	EMY (%)	AE (%)	AEf (%)	RME (%)	OE (%)	CE (%)	MP (%)
1	**4a**	86.99	72.84	83.71	72.81	72.84	87.01	86.95	3.60
2	**4b**	91.07	82.92	91.69	83.50	82.92	90.43	98.44	3.12
3	**4c**	86.72	79.03	91.47	79.32	79.03	86.39	90.57	3.00
4	**4d**	87.18	72.41	83.33	72.64	72.41	86.89	83.33	2.74
5	**4e**	88.39	81.81	92.07	81.38	81.81	88.85	97.71	3.03
6	**4f**	87.25	73.55	84.50	73.12	73.55	87.04	95.23	3.58
7	**4g**	94.48	66.29	70.34	66.45	66.29	94.24	78.57	4.72
8	**4h**	89.65	84.55	94.34	84.57	84.55	89.62	97.82	3.36
9	**4i**	87.93	82.25	94.18	82.81	82.25	87.33	94.20	3.29
10	**4j**	87.82	83.47	94.59	83.06	83.47	88.24	98.28	3.26
11	**4k**	90.47	64.04	70.88	64.12	64.04	90.34	73.77	4.49
12	**4l**	95.96	68.39	71.79	68.88	68.39	95.26	80.58	4.69
13	**4m**	88.70	63.58	71.49	63.41	63.58	88.93	71.29	4.34
14	**4n**	95.96	67.61	70.95	68.08	67.61	95.29	74.32	4.69
15	**4o**	94.26	68.04	72.41	68.25	68.04	93.96	79.41	4.54
16	**4p**	93.33	67.06	72.33	67.50	67.06	92.71	76.08	4.43
17	**4q**	95.04	68.04	71.78	68.21	68.04	94.78	75.95	4.54
18	**4r**	95.79	69.93	73.27	70.18	69.93	95.44	79.18	4.51

[a] The higher the values, the greener the process.

desired product. The conventional methodology for the synthesis of pyrazolines utilizes hazardous reactants and solvents, produces moderate product yield, requires longer reaction time, uses base and catalyst and consumes a large amount of solvent during workup of reaction, while this methodology offers high product yield, minimum utilization of toxic solvents and reagents and fast reaction time. Therefore, the calculated method ranges of AEf and AE are 63.58–83.50% and 70.34–94.59%, respectively, which are less than 100% due to the formation of water as a byproduct. For this method, the calculated CE (71.29–98.44%) is also good.

Table 5 Green metrics (PMI, MI, E-factor, and SI) of synthesized compounds (**4a–4r**)[a]

Sl no.	Product	PMI (g g^{-1})	MI (g g^{-1})	E-Factor (g g^{-1})	SI (g g^{-1})
1	**4a**	36.52	27.71	0.37	35.22
2	**4b**	31.99	31.99	0.20	30.78
3	**4c**	33.30	33.30	0.26	32.04
4	**4d**	36.45	36.45	0.38	35.07
5	**4e**	32.93	32.93	0.22	31.71
6	**4f**	36.75	27.87	0.35	35.46
7	**4g**	27.75	21.17	0.50	26.25
8	**4h**	29.74	29.74	0.18	28.55
9	**4i**	30.33	30.33	0.21	29.11
10	**4j**	30.60	30.60	0.19	29.40
11	**4k**	29.19	22.26	0.56	27.68
12	**4l**	27.98	21.29	0.46	26.52
13	**4m**	30.26	23.02	0.56	28.69
14	**4n**	27.94	21.31	0.47	26.47
15	**4o**	27.44	21.99	0.46	27.44
16	**4p**	29.66	22.56	0.49	28.17
17	**4q**	28.86	21.99	0.46	27.39
18	**4r**	29.06	22.13	0.42	27.68

[a] The lower the value, the better the process.

Reaction mass efficiency (RME) is another important metric for assessing the greenness of the process because it includes all reactant mass, AE, and yield. The RME (63.58–84.55%) and EMY (63.58–84.55%) calculations also show that the current approach has good green certification. Similarly, analyses of PMI (27.44–36.75 g g^{-1}) and MI (21.17–36.44 g g^{-1}) parameters also support this fact. The determined range of E-factors (0.18–0.56 g g^{-1}) is also found to be highly supportive of present greenness methods. Additionally, it was discovered that other green parameters were in order. The corresponding data of all coumarin-derived pyrazole–pyrazoline hybrid heterocyclic molecules are illustrated in Tables 4 and 5, and their calculations and working formulas are detailed in the SI.

Effect of solvents on fluorescence and absorption spectra of coumarin-based pyrazole–pyrazoline hybrid heterocyclic molecules

The photophysical properties of synthesized coumarin-derived pyrazole–pyrazoline hybrid heterocyclic molecules (**4a–4r**) were evaluated at room temperature through absorption and fluorescence spectroscopy in seven solvents, including acetonitrile, tetrahydrofuran, dimethyl sulfoxide, dimethyl formamide, dichloromethane, ethyl acetate and methanol, at room temperature. It was observed that most of the synthesized molecules (**4a–4r**) demonstrated an absorption maximum band in the range of 341–417 nm. The absorption maxima at 341–417 were associated with the π → π* transitions of the conjugated structure of the synthesized hybrid molecules. The effects of solvents on the absorption maxima of coumarin-derived pyrazole–pyrazoline hybrid heterocyclic molecules (**4a–4r**) are presented in Table S1 (SI). The critical assessment of the obtained results demonstrated in the table revealed that the intensity of absorption maxima decreased (hypochromic shift) with the increased polarity of
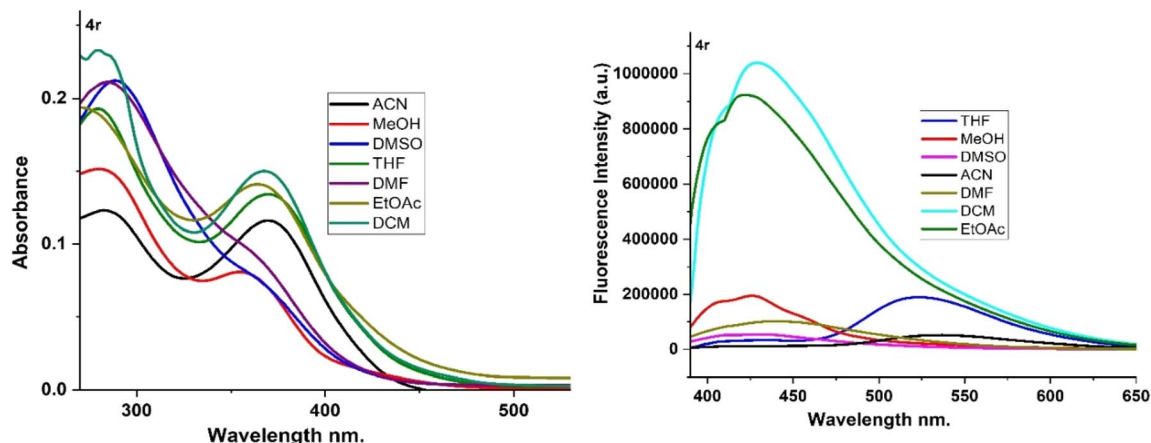
Fig. 3 UV-visible spectra of synthesized coumarin-based pyrazole–pyrazoline hybrid heterocyclic molecule (4r) in various solvents.
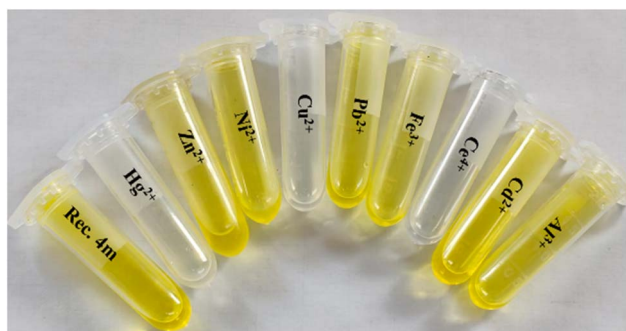

Fig. 4 Colour changes of model compound 4m for Hg^{2+}, Cu^{2+}, and Ce^{4+} ions over the other cations.

while bathochromic shifts were induced by an increase in the values of the dipole moment. It was noticed that the changes in absorption maxima were much less compared to the shift in emission maxima of the fluorescence spectra of the synthesized molecules, which suggested that the ground state of the synthesized molecules had minimal charge transfer. The red shift in emission maxima with increased polarity of solvent was higher than the red shift observed in absorption maxima, indicating that the excited state energies of coumarin-derived pyrazole–pyrazoline hybrid molecules are more influenced by the polarity of solvent compared to the ground state energies of the studied heterocyclic molecule. Additionally, the solvent polarity-dependent red shift suggested the occurrence of the π → π* transition. The shifting of emission maxima towards longer wavelength revealed the presence of notable differences between the charge distributions of the molecules in the excited and ground states probably because of stronger intermolecular interactions in polar solvents in the excited state.
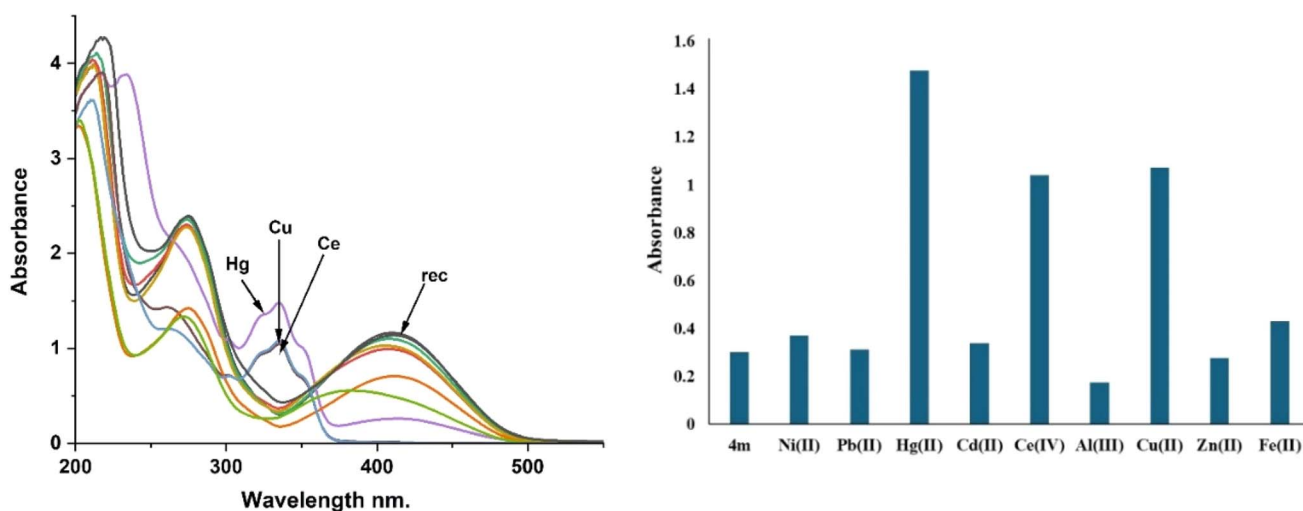
the solvents (as shown in Fig. 3). Additionally, it was found that in some cases, the absorption maxima of synthesized molecules moved to a bathochromic shift with increased polarity of solvents. The hypochromic shifts with increased polarity were the result of the formation of a hydrogen bond,

Fig. 5 UV-visible spectra of compound 4m upon the addition of Hg^{2+}, Zn^{2+}, Cu^{2+}, Ni^{2+}, Pb^{2+}, Ce^{4+}, Fe^{3+}, Cd^{2+}, and Al^{3+} ions in acetonitrile solutions.

Sensing behavior of synthesized coumarin-based pyrazole–pyrazoline hybrid heterocyclic molecules towards heavy metal ions

In our endeavour to investigate the heavy metal ion sensing characteristics of synthesized coumarin-based pyrazole–pyrazoline hybrid heterocyclic molecules (**4a–4r**), hybrid compound **4m** was selected as a model receptor, and various salt solutions of heavy metal ions were added to an acetonitrile solution of compound **4m** at room temperature. In the initial assessment, the light-yellow colour of compound **4m** solution disappeared (colourless) in the presence of individual salts of Cu^{2+}, Ce^{4+} and Hg^{2+} ions. However, no such discernible changes were observed with other metal ion salts, including Zn^{2+}, Ni^{2+}, Pb^{2+}, Fe^{3+}, Cd^{2+} and Al^{3+}, into the solution of **4m** under the same experimental conditions, as illustrated in Fig. 4. This rapid colorimetric shift helps with real-time metal ion detection by the "naked eye" without the need for any sophisticated equipment.

Further, UV-vis studies were conducted to provide quantitative information about the nature of the bonding interaction between compound **4m** and Cu^{2+}, Ce^{4+}, and Hg^{2+} ions. Compound **4m** showed two adsorption bands at 410 and 275 nm in the absorption spectrum. The binding capability of compound **4m** towards the different heavy metal ions was investigated by adding an acetonitrile solution of salts of Hg^{2+}, Zn^{2+}, Cu^{2+}, Ni^{2+}, Pb^{2+}, Ce^{4+}, Fe^{3+}, Cd^{2+}, and Al^{3+} to a 7.48×10^{-5} M solution of compound **4m**, as illustrated in Fig. 5.

As depicted in Fig. 5, by only adding Cu^{2+}, Ce^{4+}, and Hg^{2+} ions into a 7.48×10^{-5} M solution of **4m**, the peak at 410 nm was drastically decreased along with the appearance of a new peak at 336 nm with a 73 nm blue shift. This shift in absorption spectrum clearly indicated the sensing affinity of compound **4m** towards
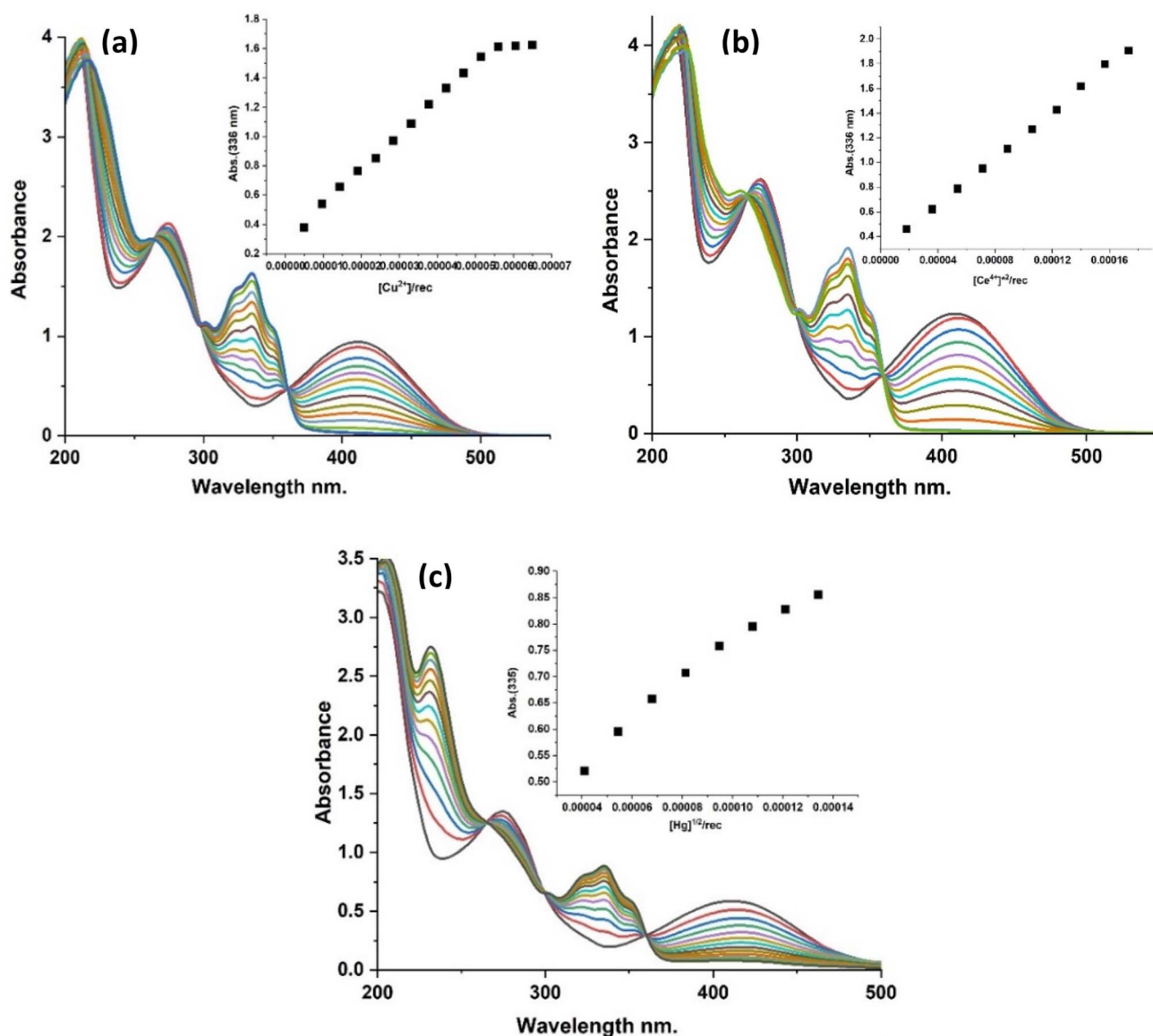

Fig. 6   UV titration spectra of receptor (**4m**) (7.48×10^{-5} M) with (a) 0–1.2 equivalent of Cu^{2+}, (b) 0–1.8 eq. Ce^{4+}, and (c) 0–0.6 eq. Hg^{2+}.

Cu^{2+}, Ce^{4+}, and Hg^{2+} ions, while no such discernible shifting was observed in absorption spectra with other ions, like Zn^{2+}, Ni^{2+}, Pb^{2+}, Fe^{3+}, Cd^{2+} and Al^{3+}, as illustrated in Fig. 5. Furthermore, to gain more insight into sensing capability, UV-visible titration experiments were performed with Cu^{2+}, Ce^{4+} and Hg^{2+} metal ion solutions in the CH_3CN solvent system. The titration experimental result revealed that the progressive addition of Cu^{2+}, Ce^{4+}, and Hg^{2+} ion solution into a 7.48×10^{-5} M solution of **4m** results in a gradual decrease in the peak at 410 nm with simultaneous evaluation of a peak at 336 nm, as shown in Fig. 6. The critical observation of the titration result demonstrated that saturation in increments of the peak at 336 was the result of the addition of one equivalent of copper ions (Fig. 6a), while a similar situation was obtained after the addition of 2.0 and 0.5 equivalents of Ce^{4+} and Hg^{2+} ions, respectively (Fig. 6b and c).

Furthermore, Job's continuous variation plots were plotted to determine the binding stoichiometry for Cu^{2+}, Ce^{4+}, and Hg^{2+} ions. The results of Job's plots revealed that the inflection point for Cu^{2+} ion was obtained at a mole fraction of 0.5, which

showed that compound **4m** interacts with Cu^{2+} ion in a 1 : 1 stoichiometry ratio, as depicted in Fig. 7a. Similarly, compound **4m** exhibited an inflection point at mole ratios of 0.3 and 0.7 for Ce^{4+} and Hg^{2+}, respectively, indicating 1 : 2 and 2 : 1 binding stoichiometries of **4m** with Ce^{4+} and Hg^{2+} ions (Fig. 7b and c).

Moreover, Benesi–Hildebrand plots were recorded with $[1/(A - A0)]$ *versus* $1/[Cu^{2+}]$, which showed a linear relationship with 0.99 correlation (R^2), clearly showing that a 1 : 1 binding stoichiometry was created between **4m** and Cu^{2+} ions. In contrast, a Benesi–Hildebrand plot showed a linear relationship between $[1/(A - A0)]$ and $1/[Ce^{4+}]$,[2] revealing a 1 : 2 binding stoichiometry between **4m** and Ce^{4+} ions. Another linear relationship was observed between absorbance $[1/(A - A0)]$ *versus* $1/[Hg^{2+}]^{1/2}$ in the Benesi–Hildebrand plot, demonstrating a 2 : 1 binding stoichiometry between **4m** and Hg^{2+} ions (Fig. 8).

Additionally, binding constants (K_f) were determined from UV-visible titration data, which were found to be 1.38×10^4 M^{-1}, 1.86×10^3 M^{-2} and 2.21×10^4 $M^{-1/2}$ for Cu^{2+}, Ce^{4+} and Hg^{2+} ions, respectively. Furthermore, to calculate the detection
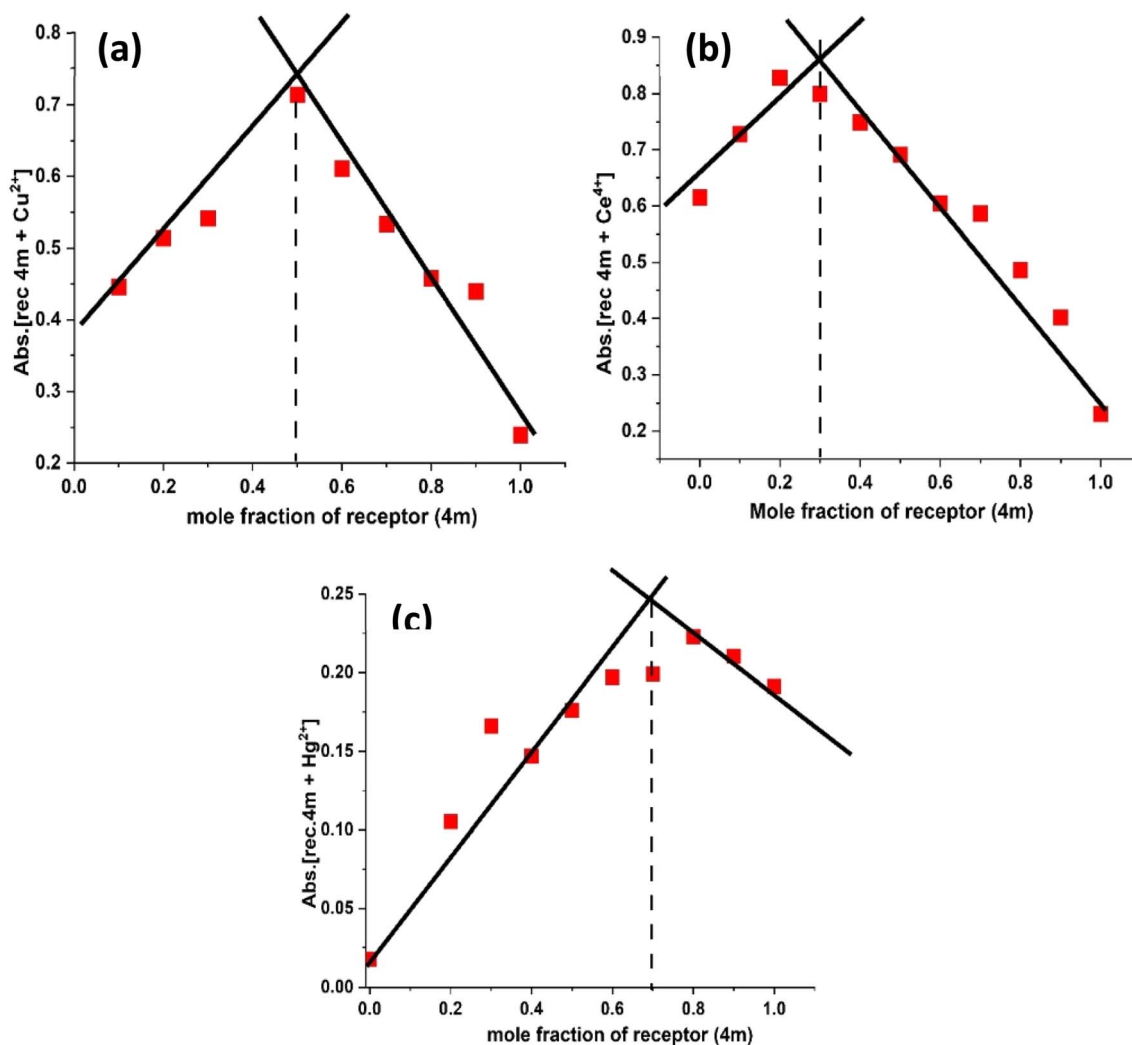

Fig. 7 Job's continuation variation graph of compound **4m** with (a) Cu^{2+}, (b) Ce^{4+} and (c) Hg^{2+} ions calculated through UV-vis experiments in a CH_3CN solution.
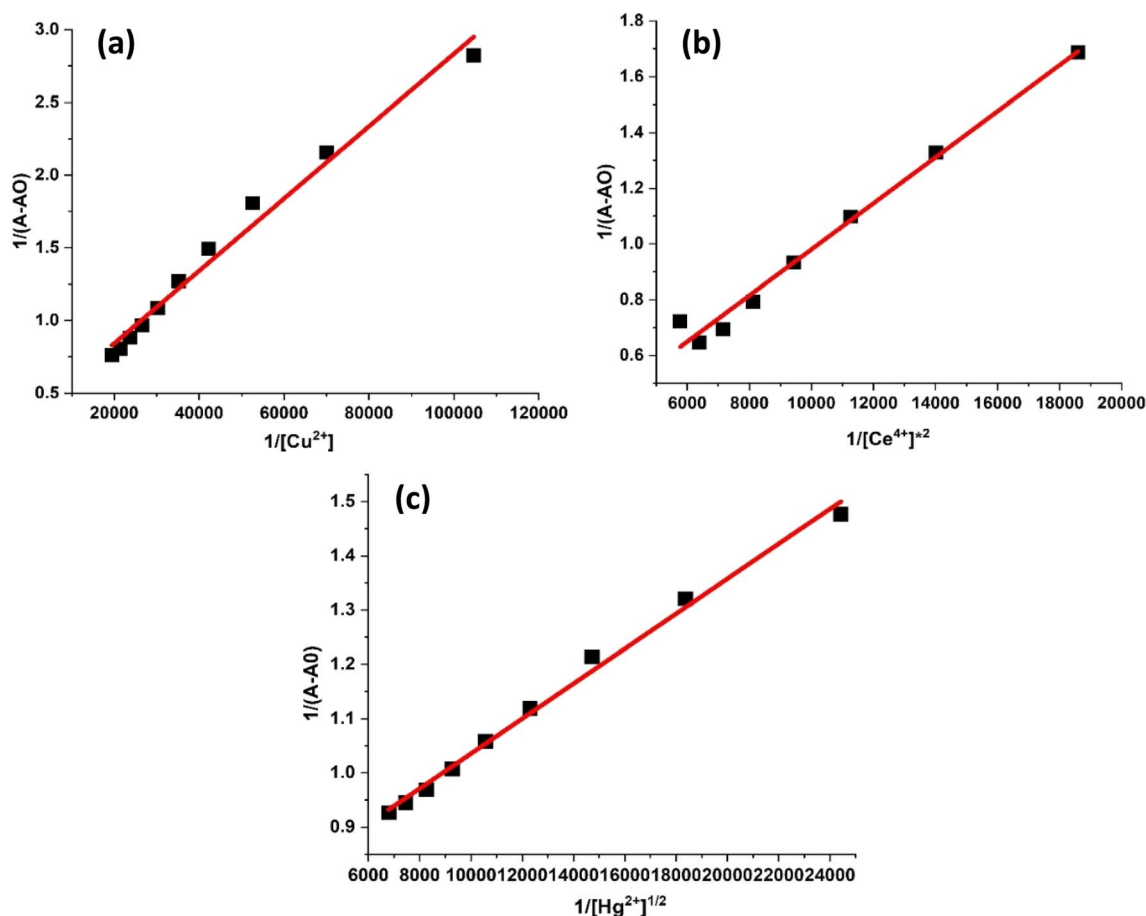
Fig. 8   Benesi–Hildebrand plot of compound **4m** with (a) Cu^{2+}, (b) Ce^{4+} and (c) Hg^{2+} ions.

Table 6   Detection limit and binding constant of other coumarin-based pyrazole–pyrazoline hybrid heterocyclic compounds with Cu^{2+}, Ce^{4+} and Hg^{2+} ions

S. no.	Compounds	Metal ion	Binding stoichiometry	Binding constant (K_f)	Detection limit
1	**4k**	Cu^{2+}	[1 : 2]	2.33×10^3 M^{-2}	4.23×10^{-8} M
2	**4n**	Hg^{2+}	[2 : 1]	4.73×10^4 M$^{-1/2}$	1.92×10^{-6} M
3	**4n**	Ce^{4+}	[1 : 1]	4.27×10^4 M^{-1}	3.09×10^{-7} M
4	**4p**	Cu^{2+}	[1 : 1]	4.70×10^4 M^{-1}	1.73×10^{-8} M
5	**4r**	Ace^{-1}	[2 : 1]	9.32×10^3 M$^{-1/2}$	3.42×10^{-7} M

limit of compound **4m** for Cu^{2+}, Ce^{4+} and Hg^{2+} ions, UV-visible absorption spectra of blank tests were measured ten times, and the standard deviation of blank readings was calculated. The linear fitting curves were plotted from the data of the titration experiment, and LOD (limits of detection) were calculated using the formula LOD = $3\alpha/S$, where S is the slope of the absorbance calibration curve and α is the standard deviation of the absorbance intensity of compound **4m** for blank measurements. The detection limits for Cu^{2+}, Ce^{4+} and Hg^{2+} ions were determined to be 5.34×10^{-8} M, 1.24×10^{-7} M and 3.03×10^{-7} M, respectively. The binding constant and detection limit of other coumarin-based pyrazole–pyrazoline hybrid heterocyclic compounds are presented in Table 6.

Further, the sensing ability of compound **4m** for Cu^{2+}, Ce^{4+}, and Hg^{2+} ions was carried out using fluorescence spectroscopy. It was observed that compound **4m** showed an emission peak at 557 nm on excitation at 410 nm, as shown in Fig. 9. More than ~99% quenching was obtained at the emission peak at 557 nm during the interaction of Cu^{2+}, Ce^{4+}, and Hg^{2+} ions, showing the capability of **4m** as a significant sensing probe for these metal ions. The observed quenching in emission maxima at 557 nm with Cu^{2+}, Ce^{4+}, and Hg^{2+} ions can be explained by intramolecular charge transfer (ICT) upon the binding of the metal ion with the pyrazoline nitrogen moiety and OH group. These studies demonstrated that compound **4m** behaves as a fluorescent chemosensor for Cu^{2+}, Ce^{4+}, and Hg^{2+} ions.
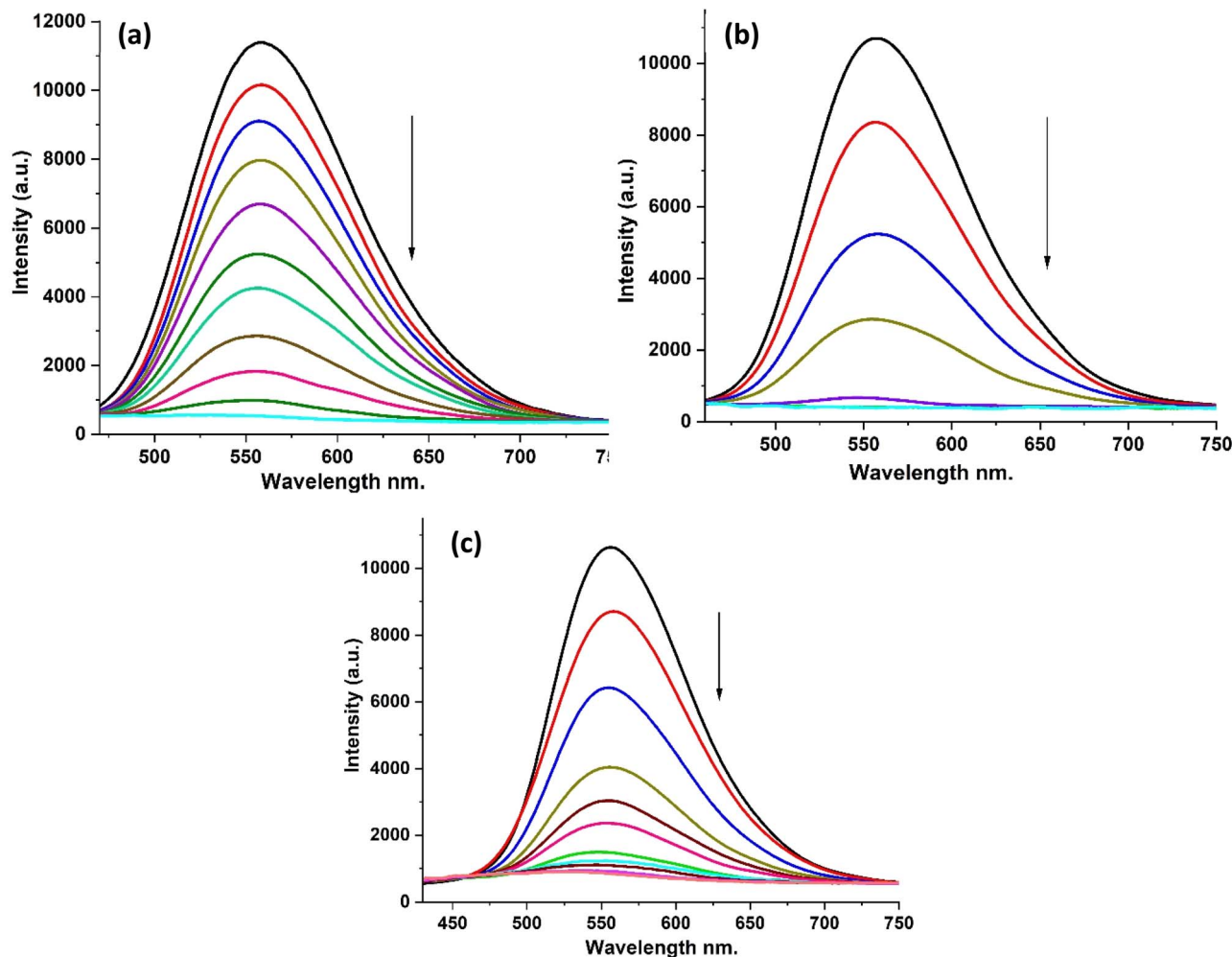
Fig. 9   Emission spectra of **4m** with (a) Cu^{2+}, (b) Ce^{4+} and (c) Hg^{2+} ions.

Conclusion

In conclusion, we synthesized a series of new coumarin-based pyrazole–pyrazoline hybrids (**4a–4r**) with 86–96% isolated yield using a molecular hybridization approach. The greenness and environmental friendliness of the reported methodology for the synthesis of multi heterocyclic compounds were assessed using various green parameters, such as atom economy, effective mass yield, atom efficiency, carbon efficiency, optimum efficiency, mass productivity, and solvent intensity. The results of these green parameter analyses revealed that the reported methodology is safe and sustainable for the environment. Apart from environmentally benign processes, operational simplicity, mild reaction conditions, avoidance of catalysts, ambient temperature, excellent product yields, and high purity without using lengthy column chromatography are some additional benefits of this approach. Further, antimicrobial and antifungal activities of synthesized hybrid molecules were examined against *E. coli*, *B. subtilis*, *S. aureus*, *C. albicans* and *A. niger* through the serial dilution method using fluconazole and ciprofloxacin as reference drugs. The obtained result

demonstrates that hybrid compounds **4c**, **4d** and **4o** exhibited maximum antibacterial activities against *B. subtilis*, *E. coli*, and *S. aureus* with MICs of 0.0132, 0.0145, and 0.0223 µmol mL^{-1}, respectively. However, **4a** and **4c** exhibited maximum potency against *C. albicans* and *A. niger*, with MICs of 0.0281 and 0.0265 µmol mL^{-1}, respectively. Results of molecular docking suggest that compound **4c** binds strongly within the active sites of enzymes 8BBX and 5TZ7 with binding energies of −10.7 and −8.9 kcal mol^{-1}, respectively, which is consistent with its strong antimicrobial potential against *A. niger* and *B. subtilis*. Moreover, sensing behaviours of synthesized multi-heterocyclic compounds (**4a–4r**) were examined, and the results indicated that most of these compounds detect Cu^{2+}, Ce^{4+} and Hg^{2+} metal ions with nanomolar detection limits. Job's plot and Benesi–Hildebrand plot demonstrated that these compounds interact with Cu^{2+}, Ce^{4+} and Hg^{2+} ions in ratios of 1 : 1, 1 : 2 and 2 : 1 binding stoichiometry, respectively. The reported tri-heterocyclic coumarin-based pyrazole–pyrazoline hybrids enhance the chemical space of bioactive hybrids but also present opportunities for future uses in sensing chemistry as selective chemosensors for biologically and environmentally

significant heavy metal ions and antimicrobial agents in medicinal chemistry. The pharmacological properties and sensing ability of these hybrids may be further improved by ongoing substitution pattern optimization and structure–activity relationship studies, providing the way for their possible translation into useful biological and analytical applications.

Conflicts of interest

There are no conflicts to declare.

Data availability

The data supporting this article have been included as part of the supplementary information (SI). Supplementary information is available. See DOI: https://doi.org/10.1039/d5ra06322a.

Acknowledgements

References

1 M. Elagawany, L. Maram and B. Elgendy, *J. Org. Chem.*, 2023, **88**(24), 17062–17068.

2 B. Das, N. Bhunia and M. Lingaiah, *Synthesis*, 2011, **21**, 3471–3474.

3 L. Maram, J. M. Michael, H. Politte, V. S. Srirama, A. Hadji, M. Habibi, M. O. Kelly, R. T. Brookheart, B. N. Finck, L. Hegazy, K. S. McCommis and B. Elgendy, *Eur. J. Med. Chem.*, 2025, **283**, 117150.

4 P. N. Kalaria, S. C. Karad and D. K. Raval, *Eur. J. Med. Chem.*, 2018, **158**, 917–936.

5 X. Y. Yu, Q. Q. Zhao, J. Chen, W. J. Xiao and J. R. Chen, *Acc. Chem. Res.*, 2020, **53**, 1066–1083.

6 L. Ravindar, S. A. Hasbullah, K. P. Rakesh and N. I. Hassan, *Eur. J. Pharm. Sci.*, 2023, **183**, 106365.

7 N. Sharma, S. Swami, S. Pathak, V. P. Verma and R. Shrivastava, *Res. Chem. Intermed.*, 2023, **49**, 3441–3459.

8 M. Faisal, A. Saeed, S. Hussain, P. Dar and F. A. Larik, *J. Chem. Sci.*, 2019, **131**, 70.

9 M. Asad, S. A. Khan, M. N. Arshad, A. M. Asiri and M. Rehan, *J. Mol. Struct.*, 2021, **1234**, 130131.

10 N. Sharma, S. Swami, V. P. Verma, R. Nair and R. Shrivastava, *J. Mol. Struct.*, 2025, **1322**, 140297.

11 A. Jamwal, A. Javed and V. Bhardwaj, *J. Pharm. BioSci.*, 2013, **3**, 114–123.

12 M. M. Ramiz, I. S. A. Hafiz, M. A. A. Reheim and H. M. Gaber, *J. Chin. Chem. Soc.*, 2012, **59**, 72–80.

13 S. K. Biswas and D. Das, *Org. Chem.*, 2022, **19**, 552–568.

14 M. A. Shamsuddin, A. H. Ali, N. H. Zakaria, M. F. Mohammat, A. S. Hamzah, Z. Shaameri, K. W. Lam, W. F. M. Lee, H. K. Agustar, M. R. M. A. Razak, J. Latip and N. I. Hassan, *Pharma*, 2021, **14**, 1174.

15 L. Ravindar, S. A. Hasbullah, K. P. Rakesh and N. I. Hassan, *Eur. J. Pharm. Sci.*, 2023, **183**, 106365.

16 H. Kiyani, H. A. Samimi, F. Ghorbani and S. Esmaieli, *Curr. Chem. Lett.*, 2013, **2**, 197–206.

17 J. W. Tessmann, J. Buss, K. R. Begnini, L. M. Berneira, F. R. Paula, C. M. P. de Pereira, T. Collares and F. K. Seixas, *Biomed. Pharmacother.*, 2017, **94**, 37–46.

18 S. Beebany, S. S. Jasim, M. M. Al-Tufah and S. S. H. Arslan, *Chem. Methodol.*, 2023, **7**, 123–136.

19 K. Manna, U. Banik, P. S. Ghosh and M. Das, *Nirma University Journal of Pharmaceutical Sciences*, 2014, **1**, 37–49.

20 M. M. Heravi, M. Daraie and V. Zadsirjan, *Mol. Diversity*, 2015, **19**, 577–623.

21 M. Hossain and A. K. Nanda, *Sci. J. Chem.*, 2018, **6**, 83–94.

22 M. J. Ahsan, *Arabian J. Chem.*, 2017, **10**, S2762–S2766.

23 F. Tok, B. İ. Abas, Ö. Çevik and B. Koçyiğit-Kaymakçıoğlu, *Bioorg. Chem.*, 2020, **102**, 104063.

24 N. Kisan Rasal, R. Bhaskar Sonawane and S. Vijay Jagtap, *Chem. Biodiversity*, 2021, **18**, e2100504.

25 G. Kumar, O. Tanwar, J. Kumar, M. Akhter, S. Sharma, C. R. Pillai, M. M. Alam and M. S. Zama, *Eur. J. Med. Chem.*, 2018, **149**, 139–147.

26 A. C. Tripathi, S. Upadhyay, S. Paliwal and S. K. Saraf, *EXCLI J.*, 2018, **17**, 126–148.

27 M. Asad, S. A. Khan, M. N. Arshad, A. M. Asiri and M. Rehan, *J. Mol. Struct.*, 2021, **1234**, 13013.

28 V. N. Badavath, I. Baysal, G. Ucar, B. N. Sinha and V. Jayaprakash, *ACS Med. Chem. Lett.*, 2016, **7**, 56–61.

29 R. Singh, S. Thota and R. Bansal, *ACS Chem. Neurosci.*, 2018, **9**, 272–283.

30 M. D. Altintop, A. Özdemir, Z. A. Kaplancikli, G. Turan-Zitouni, H. E. Temel and G. A. Çiftçi, *Archiv. Der, Pharmazie*, 2013, **346**, 189–199.

31 S. Ovais, H. Pushpalatha, G. B. Reddy, P. Rathore, R. Bashir, S. Yaseen, A. Dheyaa, R. Yaseen, O. Tanwar, M. Akthar, M. Samim and K. Javed, *Eur. J. Med. Chem.*, 2014, **80**, 209–217.

32 G. Çelik, T. Arslan, M. Şentürk and D. Ekinci, *Archiv. Der, Pharmazie*, 2020, **353**, 1900292.

33 J. H. Lange, A. Attali, M. A. van der Neut, H. C. Wals, A. Mulder, H. Zilaout, A. Duursma, H. M. van aken and B. J. van Vliet, *Bioorg. Med. Chem. Lett.*, 2010, **20**, 4992–4998.

34 P. C. Lv, D. D. Li, Q. S. Li, X. Lu, Z. P. Xiao and H. L. Zhu, *Bioorg. Med. Chem. Lett.*, 2011, **21**, 5374–5377.

35 B. Nehra, S. Rulhania, S. Jaswal, B. Kumar, G. Singh and V. Monga, *Eur. J. Med. Chem.*, 2020, **205**, 112666.

36 T. Vahedpour, M. Hamzeh-Mivehroud, S. Hemmati and S. Dastmalchi, *ChemistrySelect*, 2021, **6**, 6483–6506.

37 M. Grazul and E. Budzisz, *Coord. Chem. Rev.*, 2009, **253**, 2588–2598.

38 L. Ravindar, S. A. Hasbullah, K. P. Rakesh and N. I. Hassan, *Eur. J. Pharm. Sci.*, 2023, **183**, 106365.

39 N. H. Nasab, F. Azimian, H. G. Kruger and S. J. Kim, *Tetrahedron*, 2022, **129**, 133158.

40 A. Ibrar, S. Zaib, I. Khan, F. Jabeen, J. Iqbal and A. Saeed, *RSC Adv.*, 2015, **5**, 89919.

41 P. V. Shaikh, *Asian J. Chem.*, 2023, **35**(4), 1009–1013.

42 O. Trott and A. J. Olson, AutoDock Vina, *Comput. Chem.*, 2010, **31**, 455–461.

43 S. S. Butt, Y. Badshah, M. Shabbir and M. Rafiq, *JMIR Bioinform. Biotechnol.*, 2020, **1**, e14232.

44 M. Babu Singh, Himani, S. Yadav and P. Singh, *ChemistrySelect*, 2024, **9**, e202304767.

45 T. Brown, ChemDraw, *Sci. Tech*, 2014, **81**, 67.

46 D. S. Biovia, *Discovery Studio Visualizer*, San Diego, CA, USA, 2017, vol. 936, pp. 240–249.

47 M. B. Singh, V. K. Vishvakarma, A. A. Lal, R. Chandra, P. Jain and P. Singh, *J. Indian Chem. Soc.*, 2022, **99**, 100790.

48 S. Swami, A. Agarwala, B. Malik and R. Shrivastava, *J. Chem. Sci.*, 2016, **128**, 1451–1457.

49 A.-E. Dascălu, A. Ghinet, E. Boulanger, S. Shova and E. Lipka, *Chirality*, 2025, **37**, e70042.

50 O. Trott and A. J. Olson, *J. Comput. Chem.*, 2010, **31**, 455.